

Long- and Short-Term Stress Interaction of the 2019 Ridgecrest Sequence and Coulomb-Based Earthquake Forecasts

Shinji Toda*¹ and Ross S. Stein²

ABSTRACT

We first explore a series of retrospective earthquake interactions in southern California. We find that the four $M_w \geq 7$ shocks in the past 150 yr brought the Ridgecrest fault ~ 1 bar closer to failure. Examining the 34 hr time span between the M_w 6.4 and M_w 7.1 events, we calculate that the M_w 6.4 event brought the hypocentral region of the M_w 7.1 earthquake 0.7 bars closer to failure, with the M_w 7.1 event relieving most of the surrounding stress that was imparted by the first. We also find that the M_w 6.4 cross-fault aftershocks shut down when they fell under the stress shadow of the M_w 7.1. Together, the Ridgecrest mainshocks brought a 120 km long portion of the Garlock fault from 0.2 to 10 bars closer to failure. These results motivate our introduction of forecasts of future seismicity. Most attempts to forecast aftershocks use statistical decay models or Coulomb stress transfer. Statistical approaches require simplifying assumptions about the spatial distribution of aftershocks and their decay; Coulomb models make simplifying assumptions about the geometry of the surrounding faults, which we seek here to remove. We perform a rate-state implementation of the Coulomb stress change on focal mechanisms to capture fault complexity. After tuning the model through a learning period to improve its forecast ability, we make retrospective forecasts to assess model's predictive ability. Our forecast for the next 12 months yields a 2.3% chance of an $M_w \geq 7.5$ Garlock fault rupture. If such a rupture occurred and reached within 45 km of the San Andreas, we calculate it would raise the probability of a San Andreas rupture on the Mojave section by a factor of 150. We therefore estimate the net chance of large San Andreas earthquake in the next 12 months to be 1.15%, or about three to five times its background probability.

KEY POINTS

- Four $M_w \geq 7$ shocks during the past 150 years brought the Ridgecrest faults significantly closer to failure.
- The M_w 6.4 brought the M_w 7.1 closer to failure, with both shocks raising the stress along the Garlock fault.
- If the Garlock fault ruptured to the San Andreas, it would likely trigger a large Mojave section earthquake.

[Supplemental Material](#)

INTRODUCTION

There is abundant—but not unanimous—evidence that static Coulomb stress transfer can promote and inhibit subsequent earthquakes. To understand past interactions and to forecast future events, here we attempt to honor the complexity seen in active fault systems by removing key idealizations in Coulomb modeling.

The static Coulomb stress change, ΔCFF , caused by a mainshock with simplifying assumptions to account for pore pressure effects (King *et al.*, 1994) is

$$\Delta CFF = \Delta\tau + \mu' \Delta\sigma_n \quad (1)$$

in which $\Delta\tau$ is the shear stress change on a given fault plane (positive in the direction of fault slip), $\Delta\sigma_n$ is the fault-normal stress change (positive when unclamped), and μ' is the effective coefficient of friction (which implicitly includes the unknown pore pressure change on the fault). The Coulomb hypothesis holds that earthquakes are promoted when ΔCFF is positive,

1. International Research Institute of Disaster Science (IRIDeS), Tohoku University, Aoba, Sendai, Japan; 2. Temblor, Inc., Redwood City, California, U.S.A.

*Corresponding author: toda@irides.tohoku.ac.jp

Cite this article as Toda, S., and R. S. Stein (2020). Long- and Short-Term Stress Interaction of the 2019 Ridgecrest Sequence and Coulomb-Based Earthquake Forecasts, *Bull. Seismol. Soc. Am.* **XX**, 1–16, doi: [10.1785/0120200169](https://doi.org/10.1785/0120200169)

© Seismological Society of America

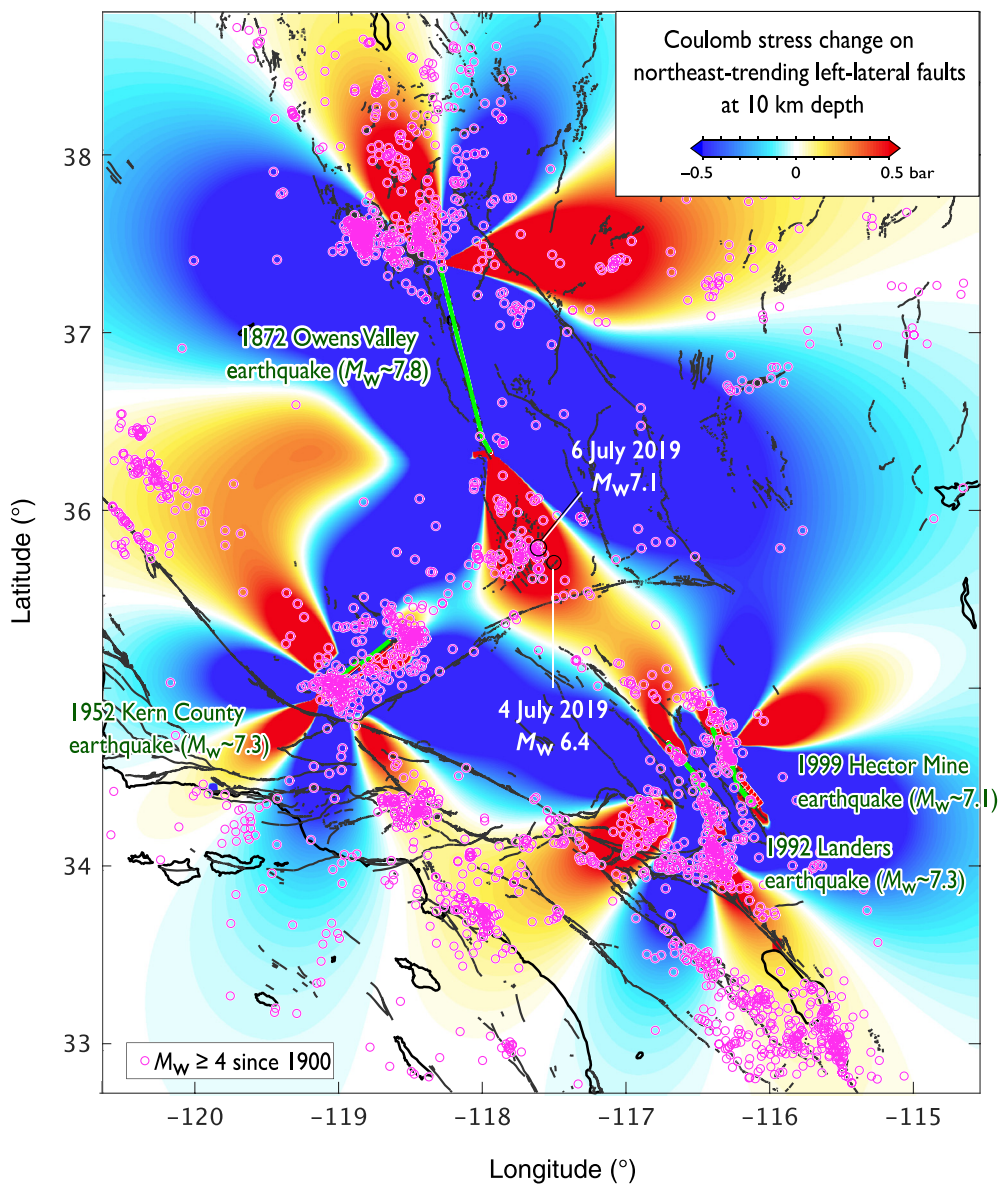


Figure 1. Stresses imparted by the largest earthquakes known to have struck within 150 km of the Ridgecrest epicenter, resolved on planes parallel to the first Ridgecrest M_w 6.4 rupture (strike/dip/rake = 228°/66°/4°). The surface projection of the rupture sources is shown by straight line segments. $M_w \geq 4$ from 1 January 1900 to 4 July 2019 (U.S. Geological Survey [USGS] Advanced National Seismic System catalog) is not a complete catalog, but the pattern would be similar if we plotted $M_w \geq 4$ since 1970, which would be complete. The color version of this figure is available only in the electronic edition.

and they are inhibited when ΔCFF is negative. In about 30,000 articles in the past 28 yr, this hypothesis has been subjected to extensive testing, in which it has been largely (e.g., Harris, 1998; Stein, 1999; Parsons *et al.*, 2012) but not exclusively (e.g., Mallman and Zoback, 2007; Steacy *et al.*, 2014; DeVries *et al.*, 2018) upheld. At the same time, it has become increasingly clear that the transient dynamic stresses transmitted by the seismic wavetrain of large earthquakes can promote, but not inhibit, fault failure. Dynamic stresses can trigger earthquakes days after the waves have disappeared, and their

effects can occur at much longer distances than for static stress (Kilb, 2003; Brodsky, 2006; Hill, 2008; Pollitz *et al.*, 2012), but in ways that are less well understood, and at this point, much harder to forecast.

Here, we seek to understand earthquake interaction in the Ridgecrest earthquake sequence, focusing first on the past 150 yr, then on the 34 hr between the two mainshocks, and finally on future earthquakes next year. Our goal is to make testable forecasts for periods of months to years, and also to ask whether the Ridgecrest earthquake could promote a Garlock fault rupture that propagates all the way to San Andreas, potentially triggering a great southern San Andreas earthquake on its section closest to Los Angeles.

STRESS TRANSFERRED BY $M_w \geq 7$ SHOCKS SINCE 1872

Was the site of the Ridgecrest sequence brought closer to failure by the large earthquakes that have struck during the past 150 yr? The 1872 $M_w \sim 7.6$ –7.9 Owens Valley (Beanland and Clark, 1994; Savage and Lisowski, 1995; Hough and Hutton, 2008), 1952 M_w 7.3 Kern County (Stein and Thatcher, 1981; Bawden, 2001), the 1992 M_w 7.3 Landers (King *et al.*, 1994; Wald and Heaton, 1994), and 1999 M_w 7.1 Hector

Mine (Dreger and Kaverina, 2000; Salichon *et al.*, 2004) earthquakes all struck within 150 km of the Ridgecrest mainshocks. In Figure 1, we sum the stress transferred by these earthquakes on receiver faults oriented as those in the 4 July 2019 M_w 6.4 Ridgecrest earthquake (left-lateral slip on a northeast-trending surface). We find that the four $M_w \geq 7$ shocks contributed to a stress increase of 0.72 ± 0.25 bars on the M_w 6.4 nucleation patch, and 0.96 ± 0.28 bars on the M_w 7.1 nucleation patch (for fault friction of 0.0–0.8), with the 1872 earthquake furnishing the most (0.24–0.90 bars). However, if we go further back to the 1857

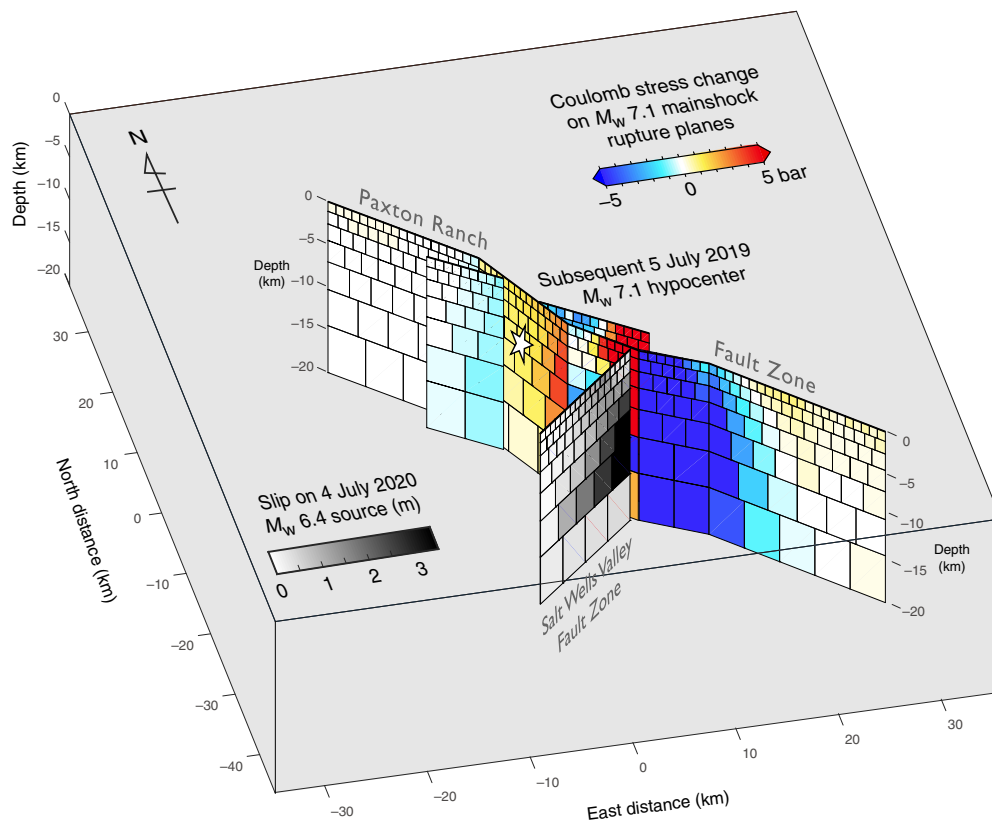


Figure 2. Coulomb stress change imparted by the M_w 6.4 earthquake to the future rupture surface of the M_w 7.1 earthquake. The stress increase in the vicinity of the M_w 7.1 hypocenter is about 0.5–1.0 bar. Note that larger stress increases occurred closer to the M_w 6.4 rupture surface; we do not know why the M_w 7.1 did not nucleate there. The color version of this figure is available only in the electronic edition.

$M_w \sim 7.9$ Fort Tejon earthquake (Grant and Sieh, 1993; Grant and Donnellan, 1994; Lin and Stein, 2004; Zielke *et al.*, 2012), the stress increase is reduced by 0.11 bar (Fig. S1, available in the supplemental material to this article). The full range of calculated stress changes for different source models and fault friction is given in Table S1.

Equally intriguing, the $M_w \geq 4$ seismicity shown in Figure 1 largely occurs in areas of stress increase from these four earthquakes, and are generally absent in their stress shadows. Thus, despite the existence of diverse fault orientations in southern California, and the occurrence of other large mainshocks, the stress calculation we show in Figure 1 might be a reasonable representation of the processes that promote and inhibit seismicity. We are not arguing that the four $M_w \geq 7$ events during the past 150 yr caused the Ridgecrest earthquakes, but only that their occurrence brought the Ridgecrest nucleation sites closer to failure, and they also appear to have influenced the much greater number of small southern California events.

STRESS TRANSFERRED BY THE M_w 6.4 TO THE M_w 7.1 EVENT AND CHANGES IN SEISMICITY RATE

Next, we examine the stress imparted by the 4 July 2019 M_w 6.4 earthquake to the rupture surface of the M_w 7.1 as imaged by

Xu *et al.* (2020); this is shown in perspective view in Figure 2, and in map view at a depth of 8 km (the nominal depth of the M_w 7.1 hypocenter) in Figure 3. The hypocentral patch was brought 0.66 bar closer to failure by the M_w 6.4 earthquake, and the surrounding $\sim 5 \times 20$ km patch of the future rupture was brought >2 bar closer to failure, so the increase is not restricted to the hypocenter. In contrast, the southern portion of the M_w 7.1 rupture surface was inhibited by >5 bars; presumably this was overcome by the much larger dynamic stresses shed off the M_w 7.1 rupture front as it propagated southward. Rollins *et al.* (2019) published a preliminary analysis two days after the M_w 7.1 using simple finite sources and reached similar conclusions to those shown here. Barnhart *et al.* (2019) and Goldberg *et al.* (2020) also found ~ 1 bar stress increase at the M_w 7.1 hypocenter.

Just 2.5 km from the hypocenter of the M_w 7.1, an M_w 5.4 shock struck 17.5 hr after the M_w 6.4, 16.2 hr before the M_w 7.1 (Fig. 3). Although the stress imparted by the M_w 5.4 to the M_w 7.1 hypocenter is sensitive to its unknown rupture dimensions, location uncertainties, and the strike of the M_w 5.4 fault, it was likely at least several bars, or higher than that of the M_w 6.4. So, perhaps the 34 hr delay is in some sense a product of a cascade of aftershocks, and not strictly the stress transfer from the first mainshock to the second.

Not only was the site of the M_w 7.1 hypocenter promoted by stress transfer, but seismicity in areas that were inhibited by the M_w 7.1 shut down immediately afterward. We identify two boxes of aftershocks of the M_w 6.4 earthquake that underwent sudden changes after the M_w 7.1 event (Fig. 4a,b). In box A, along the Paxton Ranch Fault Zone (also called the Ridgecrest fault), the seismicity rate jumped after the M_w 7.1 event (Fig. 5a). In box B, along the Salt Wells Valley Fault Zone (the southwest-trending cross fault), seismicity nearly shutdown after the M_w 7.1 (Fig. 5b). Box A lies in a zone of stress increases and decreases, whereas box B fell into a stress shadow (Fig. 4c). Although box A contains areas of stress increase and decrease, in the blue areas, the relative rate can only drop from one to zero, whereas in the red areas, the rate can increase from one to 100, and so in a

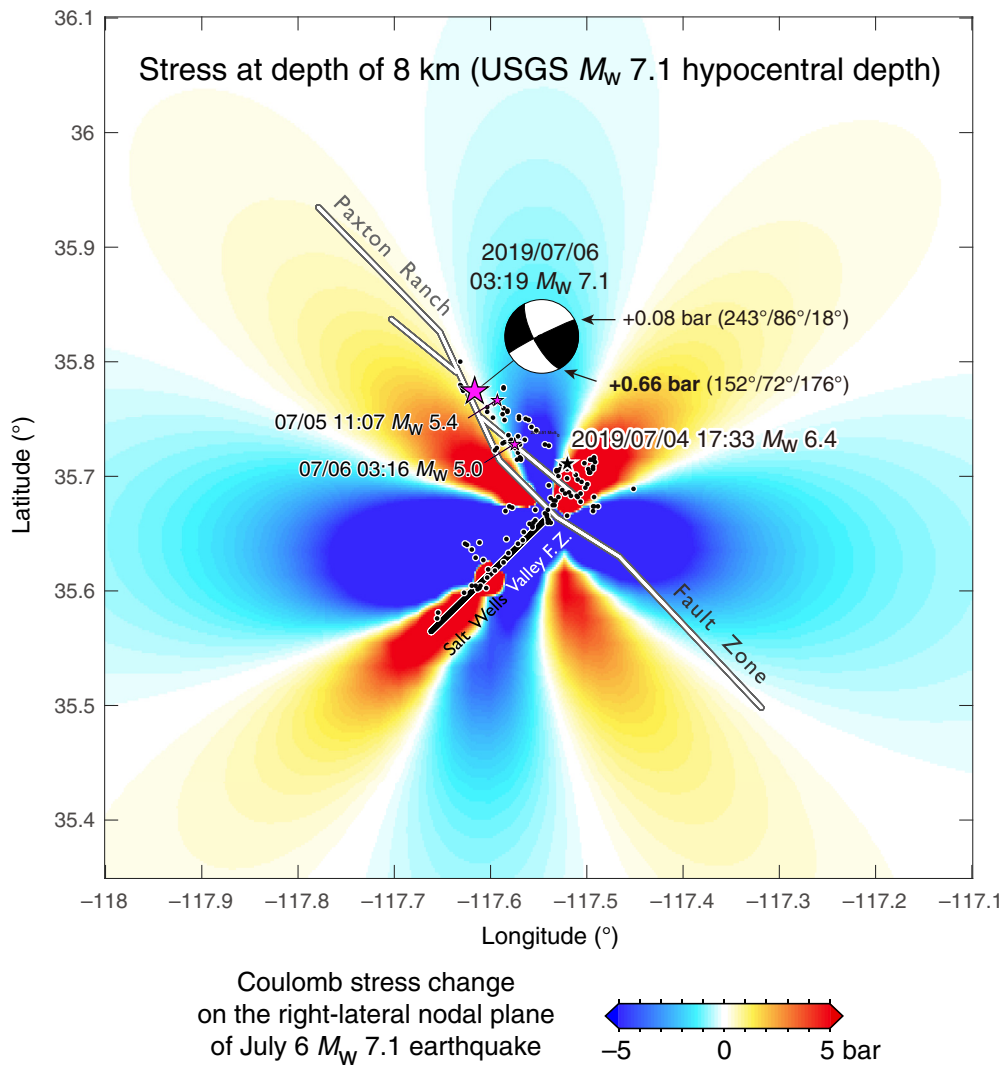


Figure 3. Coulomb stress change resolved on the right-lateral nodal plane of the M_w 7.1 earthquake, with the M_w 7.1 rupture surfaces of Xu *et al.* (2020) shown (inscribed lines), as well as all recorded shocks relocated by the Hauksson *et al.* (2012) algorithm during the 34 hr between the two main shocks (dots and stars). There is a large stress increase on the most likely nodal plane of the M_w 7.1 focal mechanism, but neither the M_w 5.0 nor M_w 5.4 aftershocks that occurred before the M_w 7.1 struck locate in the highly stressed region, perhaps indicative of the limitations of the finite fault model. USGS, U.S. Geological Survey. The color version of this figure is available only in the electronic edition.

mixed zone, there is a net rate increase (Toda *et al.*, 2012). A shutdown of cross-fault seismicity was also seen in the 1987 Superstition Hills earthquake sequence (Hudnut *et al.*, 1989), and the 1997 Kagoshima couplet (Toda and Stein, 2003).

STRESS TRANSFERRED BY THE RIDGECREST SEQUENCE TO THE GARLOCK AND OTHER MAJOR FAULTS

One way to examine the stress imparted to the principal faults surrounding the Ridgecrest source is to use planar rectangular surfaces that correspond roughly to their surface traces (Fig. 6). West of the Ridgecrest rupture, a 25 km long section Garlock fault has a large (5–10 bar) stress increase, a 25 km long section

east of the rupture has an equally large decrease, and a 50 km long westernmost section has small (~ 0.2 bar) increases. There is no evidence that the Garlock slipped at depth in response to these large calculated stress increases. Up to 20 mm of shallow left-lateral creep was detected by Interferometric Synthetic Aperture Radar (Barnhart *et al.*, 2019; Ross *et al.*, 2019) on the Garlock fault (Fig. 6b), perhaps a result of the imparted stress, as advocated by Barnhart *et al.* (2019), or perhaps due to superficial shaking. Moderate stress increases are calculated along the northern portions of the Panamint Valley and Sierra Nevada Frontal faults, as well as most of the Blackwater fault and the northern portion of the Lenwood fault.

Here, we propose an alternative way to infer the stress transferred to the Garlock fault, by calculating the stress imparted to all available focal mechanisms, regardless of time period, within 10 km of the fault trace. Although the faults on which such earthquakes occur can be small, these mechanisms provide a richer and more realistic indication of the distribution, geometry, and rake of active faults and so better capture their true complexity.

Even nominally straight, isolated, and high-slip-rate faults, such as the central San Andreas, Alpine, and North Anatolian faults, exhibit astonishing complexity when viewed by their focal mechanisms, by double-difference relocated seismicity, or by seismic reflection profiles. That complexity has many roots, including diverse fault orientations caused by the stress evolving over geologic time; by fault bends, breaks, and junctions; by fault obliquity to the plate motion; and by contrasting crustal properties and crustal fluids, all of which Robert E. Wallace stressed in Figure 7. We used the Southern California Earthquake Center (SCEC) hypocenter catalog (Hauksson *et al.*, 2012) and SCEC focal mechanism catalog (Yang *et al.*, 2012), as updated through 31 December 2019. Figure S2 shows the catalog magnitude of

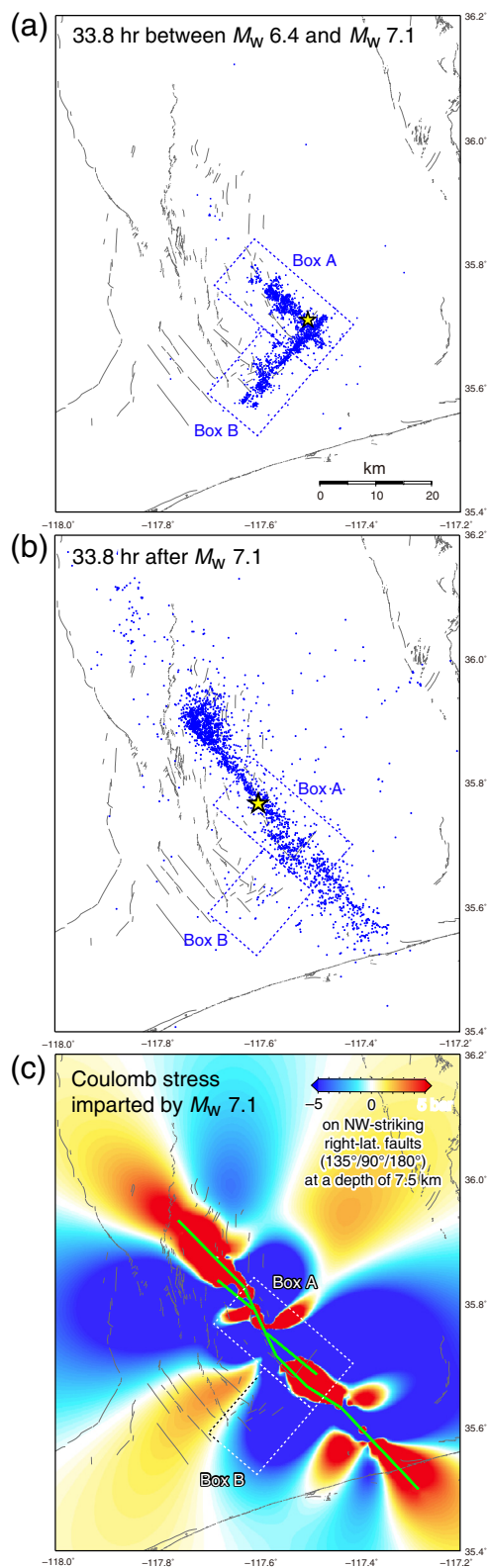


Figure 4. (a) Seismicity during the 34 hr before the M_w 7.1 (4 July 2019 17:33:49 to 6 July 2019 03:19:52 (UTC) and (b) the 34 h after (6 July 2019 03:19:52 to 7 July 2019 13:05:57 (UTC) the M_w 7.1, compared to (c) a simple model of Coulomb stress imparted by the M_w 7.1 earthquake. All detected magnitudes are plotted. NW, northwest. The color version of this figure is available only in the electronic edition.

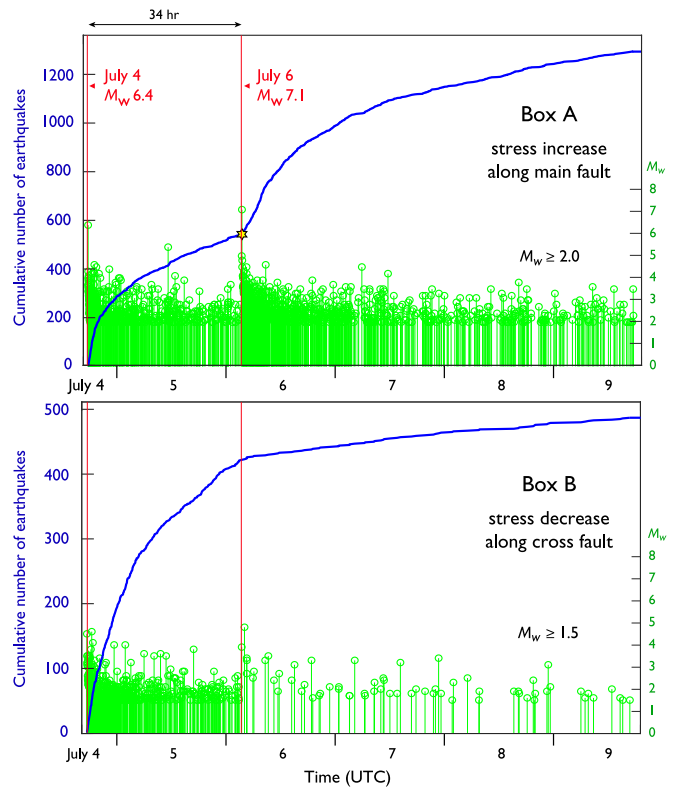


Figure 5. Seismicity time series for the events in box A and B shown in Figure 4, showing the sudden seismicity rate gain in box A, and the drop in the M_w 7.1 stress shadow in box B. The color version of this figure is available only in the electronic edition.

completeness (M_c) as a function of time. Because the magnitude of completeness, M_c , for the focal mechanism catalog is $M_w > 2$ (red curve in Fig. S2), we use the hypocenter locations of Hauksson for which $M_c \cong 2$ (blue curve in Fig. S2), assigning them Yang's mechanisms.

Although focal mechanisms may better reflect the 3D and fractal nature of fault networks than simple continuous surfaces, for non-zero fault friction there is a nodal plane ambiguity, because the Coulomb stress is not the same on orthogonal planes. So, here, we use the plane on which the Coulomb stress is most positive. This introduces a red bias (because stress increases are colored in red), which carries two intrinsic benefits: the first is that calculation of seismicity rate change, to which the stress changes will be compared in testing, is also red-biased because it is easier to measure seismicity rate increase than a decrease for all but long time periods, and so such seismicity rate change calculations are always also red biased. The second benefit is that using the plane with the most positive stress change, focal mechanisms with stress decreases (blue focal mechanism plots) must lie in the stress shadow; the stress decrease cannot be an artifact of nodal plane selection.

We show stress transferred to focal mechanisms by the M_w 6.4 and the M_w 7.1 events in Figure 8. This covers areas

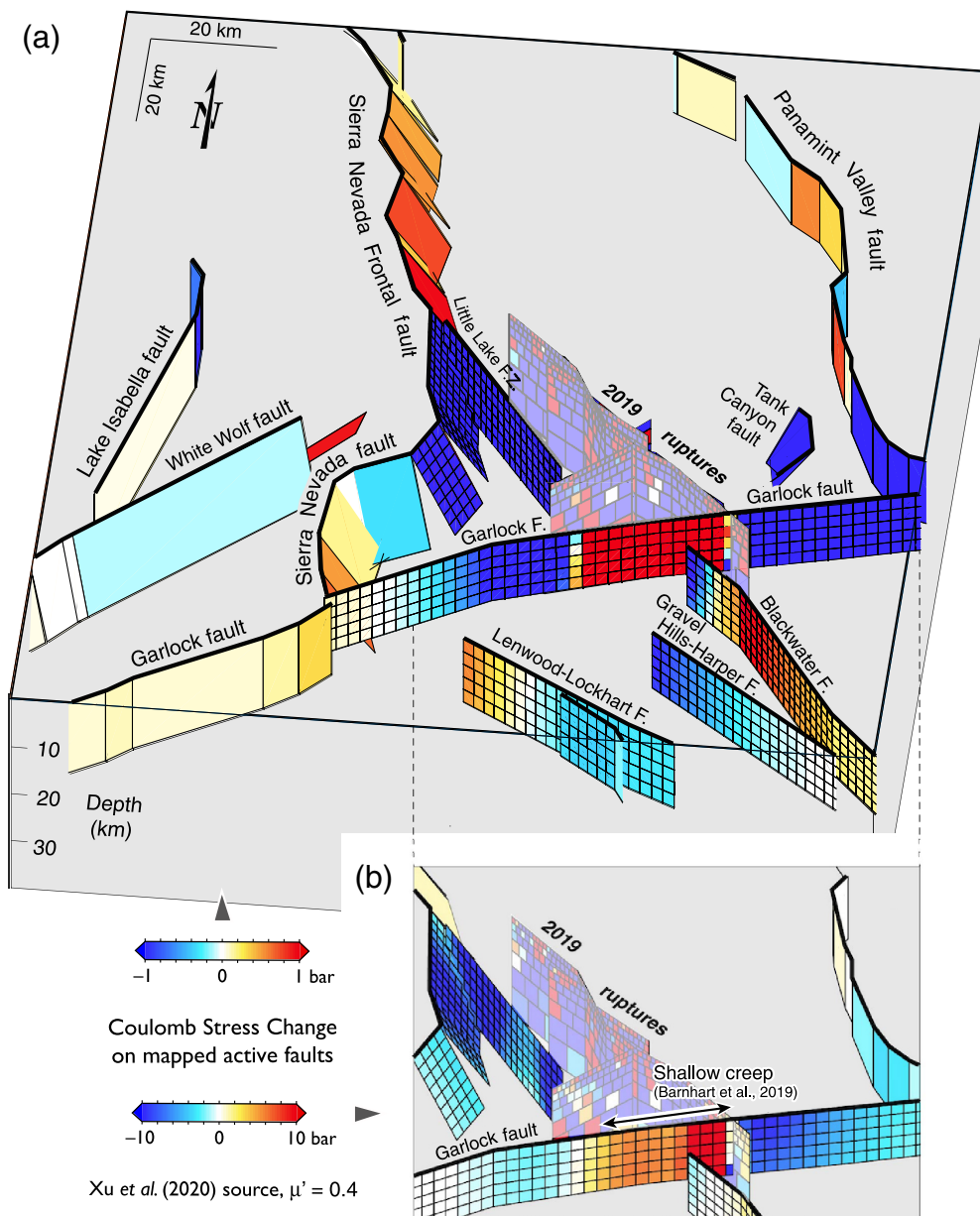


Figure 6. (a) Coulomb stresses resolved on simplified planar surfaces of the Southern California Earthquake Center (SCEC) Community Fault Model (Plesch et al., 2007) used by Uniform California Earthquake Rupture Forecast version 3; these are idealizations guided by the mapped surface traces of the major faults. The Xu et al. (2020) source model is used. (b) Stress rescaled so that the large changes on the Garlock fault are less saturated. Figure S5 shows the same calculation using the Ross et al. (2019) source model, for which only the combined M_w 6.4 + M_w 7.1 slip model is judged reliable by its authors. The color version of this figure is available only in the electronic edition.

both on and off the mapped faults—recognizing, of course, that the Ridgecrest fault itself was not previously mapped as a through-going feature. Mechanisms close to the Blackwater and Harper faults were brought closer to failure by both Ridgecrest mainshocks, while the central Sierra Nevada Frontal fault was inhibited by both events, and we believe those fault planes are a better proxy for Blackwater and Harper faults than idealized surfaces. North of the M_w 6.4 rupture (Fig. 8a), events

are red (stress increased); after the M_w 7.1 (Fig. 8b) they turn blue (stress decreased). Viewed this way, the second event is seen to be a response to the stress increases of the first throughout the nearby crust and not just at the M_w 7.1 hypocenter.

In contrast to other regions, both mainshocks brought the majority of the mechanisms along the Garlock fault closer to failure (Fig. 8a,b), with the central Garlock most stressed by the M_w 6.4, and the western Garlock most stressed by the M_w 7.1 (Fig. 8c). In total, about 120 km of the fault zone was brought ≥ 0.1 bar closer to failure when viewed from the associated focal mechanisms, in contrast to how the Garlock is seen when resolved on simple planar surfaces in Figure 6. To assess the likelihood of a Garlock rupture, and its consequences on the San Andreas, we develop a forecast method.

RETROSPECTIVE AND PROSPECTIVE AFTERSHOCK FORECASTS

Our ultimate goal is to develop testable earthquake forecasts, whose elements we outline in the following section.

Capturing fault complexity through focal mechanisms

For the earthquake rupture, we use finite-fault models (a grid of patches, each with slip and rake) as the source for the

stress. As suggested by Figure 8, we use focal mechanisms of background shocks and aftershocks as proxies for active faults, calculating the imparted stress at their hypocenters. Resolving stress on focal mechanisms was introduced by Hardebeck et al. (1998) to analyze the 1992 Landers and 1994 Northridge earthquakes. Subsequently, Ma et al. (2005) used them for the 1999 M_w 7.6 Chi-Chi earthquake, and Toda et al. (2012) used them to probe the 1992 M_w 7.3 Landers stress shadow.

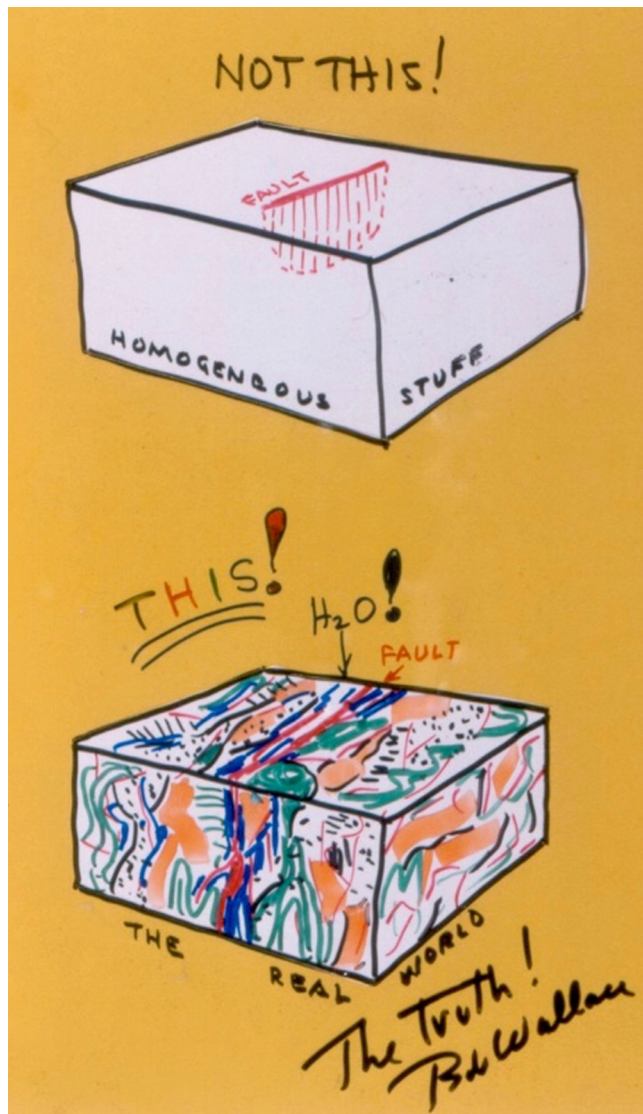


Figure 7. Some 30 yrs ago, the senior author was gently remonstrated by Robert E. Wallace, the father of paleoseismology, for drastically oversimplifying faulting in the author's models of stress transfer. In this article, we are working to take this advice at least partly to heart. The color version of this figure is available only in the electronic edition.

Even for dense seismic networks, such as in Japan, New Zealand, and California, the distribution of focal mechanisms is often sparse. Global Centroid Moment Tensor focal mechanisms (Ekström *et al.*, 2012) are generally available for $M_w \geq 5$ shocks, although some national catalogs furnish mechanisms for shocks as small as $M_w \geq 3$ (e.g., National Research Institute for Earth Science and Disaster Resilience F-net in Japan). So, we densify the data with synthetic focal mechanisms: For shocks without a mechanism, we assign the closest mechanism. This acts both to densify and smooth the receiver faults, the planes on which we resolve the imparted stress. In a manner resembling ours, Segou and Parsons (2020) found that for the 2010 M_w 7.2 El Mayor–Cucapah event, 89% of its aftershocks

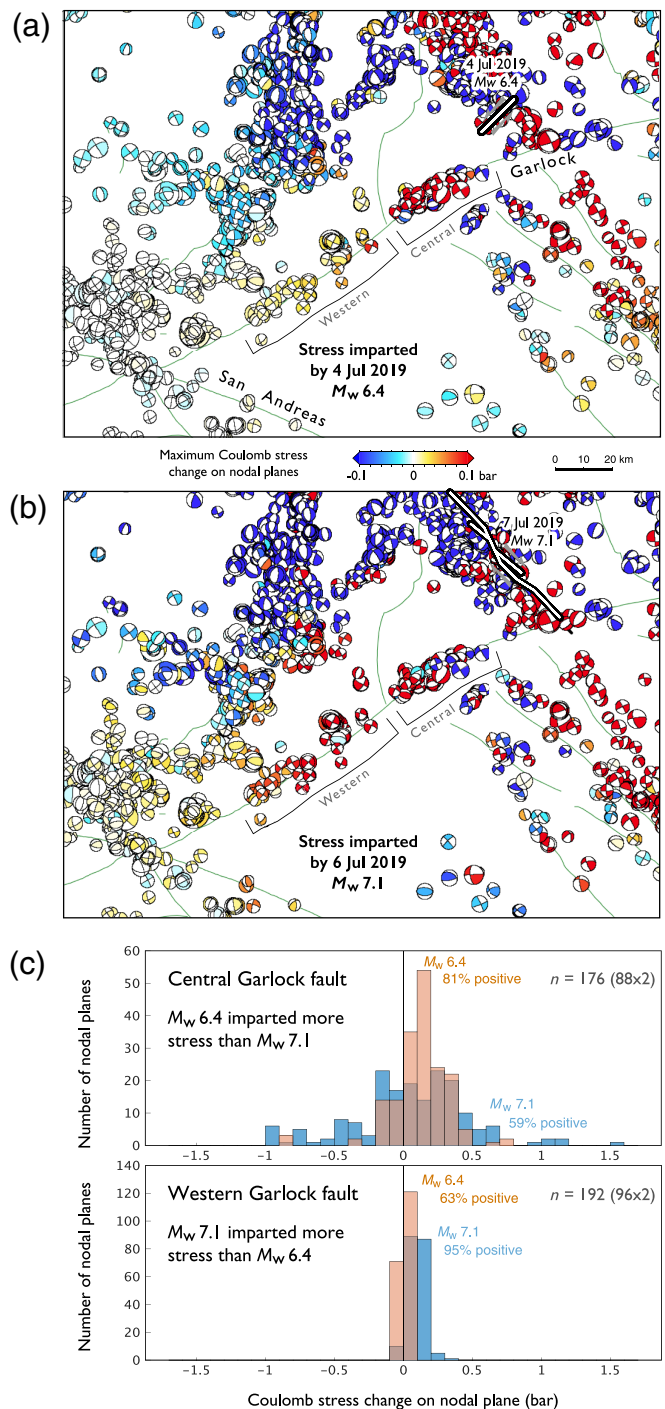


Figure 8. Coulomb stress imparted by the (a) M_w 6.4 shock and the (b) M_w 7.1 shock resolved on background focal mechanisms (synthetic mechanisms of $M_w \geq 2.0$ earthquakes from the SCEC hypocenter catalog, and the focal mechanism catalog of Yang *et al.* [2012] from 1981.0 to 1992.0), under the assumption that fault friction = 0.4. Resolved stress is color-coded onto the compressional quadrants of each focal mechanism plots. For each set of nodal planes, we plot the stress on the plane with the most positive stress change, so these plots are positive-biased. Nevertheless, there are large areas with stress decreases (focal mechanism plots with stress decreases). The stronger central Garlock stressing by M_w 6.4, and western Garlock by M_w 7.1 is evident in (c). The color version of this figure is available only in the electronic edition.

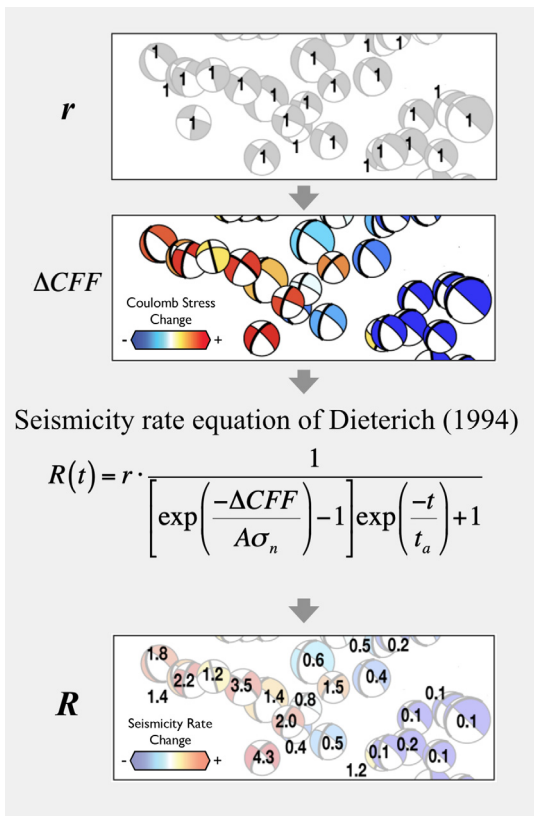


Figure 9. Schematic illustration of rate and state friction on background focal mechanisms to calculate expected seismicity rate changes. During the background period, each focal mechanism is a proxy for a small-to-moderate fault (top panel). These earthquakes then receive coseismic stress from a nearby mainshock in the second panel. That stress amplifies or diminishes seismicity rates (bottom panel). Finally, to make a map of aftershock forecast like Figure 11, the updated numbers on the focal mechanism plots in the bottom panel are spatially smoothed by a moving kernel on the grid nodes. The color version of this figure is available only in the electronic edition.

were promoted on one of the nodal planes of the closest mechanism to each aftershock.

Calculating earthquake rate changes from stress changes

We use the theory of rate-and-state friction (Dieterich, 1994) to forecast the seismicity rate change at each focal mechanism plots (Fig. 9). Here, the background rate is amplified if the stress change is positive, or suppressed if it is negative, so one must first produce background seismicity map using all synthetic focal mechanisms above the magnitude of completeness. This can be estimated from the pre-mainshock catalog at its completeness level (Woessner and Wiemer, 2005).

In addition to the background seismicity rate, background and aftershock focal mechanisms, and the mainshock finite fault models, the earthquake forecasts depend on two parameters in the seismicity rate equation of Dieterich (1994): the aftershock duration, t_a , and a constitutive parameter times

the effective normal stress, $A\sigma$. Since t_a is the time until the earthquake rate decays back to the pre-mainshock rate, it is measurable with sufficient data. Alternatively, one can use a global average of about 10 yr (Parsons, 2002), although this estimate is likely biased toward rapid aftershock decay in subduction zones; continental durations are longer. $A\sigma$ is then found by fitting the observed number of aftershocks to the forecast number; typical $A\sigma$ values are 0.1–0.5 bar.

In rate–state friction, large stress increases close to the rupture surface yield unrealistically high calculated seismicity rate immediately after stress changes because of the exponential terms in the Dieterich equation (Fig. 9). As a result, we would predict far too many near-fault aftershocks. To overcome this, we impose an arbitrary maximum stress change of 3 bars, or about 10% of a typical earthquake stress drop. Regions far from the source that have low rates of seismicity will also have few focal mechanisms, making the receiver fault geometry uncertain, a problem which is ameliorated but not solved by our use of nearest-neighbor synthetic mechanisms. Finally, although the rate–state parameters (t_a and $A\sigma$) are probably heterogeneous, we take them to be uniform. We use 20 yr and 0.2 bar, respectively.

Including stress effects of sequential earthquakes

To incorporate successive stress changes imparted by multiple mainshocks, we use the expression for seismicity rate, R , as a function of the state variable γ under a tectonic shear stressing rate $\dot{\tau}_r$ from Dieterich (1994), as implemented by Toda *et al.* (2005). Under constant shear stressing rate, the state variable reaches the steady state:

$$\gamma_0 = \frac{1}{\dot{\tau}_r}. \quad (2)$$

In the absence of a stress perturbation, the seismicity rate is assumed constant. At steady state, the seismicity rate R is equivalent to the background rate r because R is calculated from

$$R = \frac{r}{\gamma \dot{\tau}_r}. \quad (3)$$

We index the state variable γ with time. An earthquake imposes a sudden stress step ΔCFF , and so the state variable γ_{n-1} changes to a new value γ_n :

$$\gamma_n = \gamma_{n-1} \exp\left(\frac{-\Delta CFF}{A\sigma}\right). \quad (4)$$

To seek the seismicity at the time of the stress step, we substitute the new state variable in equation (4). A stress increase on a fault causes γ to drop, so the fault slips at a higher rate, yielding a higher seismicity rate. Conversely, a sudden stress drop causes γ to jump, lowering the seismicity rate. The

seismicity rate change is transient and eventually recovers, corresponding to a gradual evolution of γ , which for the next time step Δt is given by

$$\gamma_{n+1} = \left[\gamma_n - \frac{1}{\tau_r} \right] \exp \left[\frac{-\Delta t \dot{\tau}_r}{A\sigma} \right] + \frac{1}{\tau_r}. \quad (5)$$

Although the stress changes are permanent, their effect on seismicity is transient. The duration of the transient is inversely proportional to the fault stressing rate $\dot{\tau}_r$. Given sufficient time (e.g., decades to centuries), the effect of all but the largest stress changes disappear on all but the most slowly stressed faults. What is more, the lower γ is at the time of a new stress jump, the more strongly the seismicity rate will be amplified, a central element of the fault system rupture simulation software, RSQsim (Richards-Dinger and Dieterich, 2012).

Background, learning period, and forecast periods

To produce the best rate estimate, the background should contain as many earthquakes as possible. But the farther back one goes in time, the higher the magnitude of completeness, M_c , which reduces the number of usable earthquakes for the entire period. In practice, a background duration of 10–20 yr tends to yield the greatest number of earthquakes above M_c . We count synthetic earthquakes with assigned focal mechanisms in a cylinder of radius 10 km at each regular grid, and then normalize the count to avoid the effect of the overlapping cylinders. The larger the radius, the smoother the map. Each background mechanism, as a proxy of background fault plane, receives a coseismic stress change, and then the rate is amplified or diminished by the rate–state equation (Fig. 9). Finally, we map the forecast rates using the same smoothing cylinder. The background uses 1981.0–1992.0 $M_w \geq 2$ events.

To increase the fidelity of the forecasts, we use a learning period. This period compares the observed and forecast changes in seismicity rate for past moderate or larger earthquakes since 1992 (Fig. 10a and Table 1). The data-model misfit is then minimized by modifying the background rate for each calculation cell (Fig. 10b).

Spatially variable b -value

Because small shocks are much more numerous than large ones, our method essentially uses the observed rate of small shocks, amplified by stress transfer, to forecast the probability of large ones. This means that the Gutenberg–Richter relation (b -value), which controls the ratio of small to large earthquakes, matters. We find that our retrospective forecasts significantly improve when we let the b -value be spatially variable. We estimate b -value following the maximum-likelihood method of Aki (1965) using 10 or more background earthquakes within 10 km radius overlapping cylinders centered on $0.05^\circ \times 0.05^\circ$ nodes; cells with fewer than 10 earthquakes default to $b = 0.9$ (Fig. S3a).

EARTHQUAKE FORECASTS

Retrospective forecast for first 6 months since M_w 7.1

A six-month retrospective forecast (6 July–31 December 2019) was carried out first for $M_w \geq 2$ earthquakes because the b -value does not come into play, and because it yields the largest number of observations to compare with the forecast (Fig. 11). Their distribution yields a spatial regression coefficient of 0.69 and a slope of 0.83 (Fig. S4c), which we regard as encouraging, although only 54% of those we forecast took place. Notice in Figure 11 that the forecast side lobe east of the rupture is much stronger than the lobe to the west, consistent with the observed seismicity. In the GF box in Figure 11 straddling the Garlock fault, we forecast a zone of seismicity increase which occurred, even though the idealized Garlock fault there undergoes a large stress decrease (Fig. 6). But the forecast zone of seismicity south of the Garlock fault (box SG) is nearly devoid of shocks. The Garlock has slipped a total of 64 km (Monastero *et al.*, 1997), juxtaposing mostly granitic rocks to the north against mostly volcanic rocks to the south. Toda and Stein (2019) explained the absence of earthquakes south of the Garlock fault by positing that the crust south of the Garlock might be stiffer, with a higher elastic modulus.

Prospective forecast for the next 12 months

We now make a forecast for the ensuing year, 1 April 2020 to 31 March 2021 (Fig. 12). We present this first for $M_w \geq 2$ earthquakes, which uses all the elements in our approach except the variable b -value (Fig. 12a). Then, we make a $M_w \geq 7$ forecast, which incorporates variable b -values (the forecast at a lower saturation scale is shown in Fig. S3b). By summing the cells within 10 km of the Garlock fault, we estimate a 2.3% probability of an $M_w \geq 7.7$ Garlock earthquake in the next 12 months. We can compare this to the time-dependent Uniform California Earthquake Rupture Forecast version 3 (UCERF3; Field *et al.*, 2015), which gives a 0.023% probability of an $M_w \geq 7.7$ Garlock fault rupture (fig. 10 of Field *et al.*, 2015). So, the stress transfer causes a 100-fold increase in its annual occurrence likelihood. We should add that in the retrospective forecast for the first 6 months, we calculate an 8% probability of a Garlock $M_w \geq 7.7$, and of course, this did not occur.

Could a large Garlock rupture trigger a southern San Andreas event?

The Garlock fault appears to have ruptured in large earthquakes during the past 600 yr, and so could presumably do so again. McGill and Sieh (1993) and Dawson *et al.* (2003) found evidence for large events during A.D. 1450–1640, and 1490–1810 along the central section of the Garlock fault, for which they infer 5–8 mm/yr slip rates. Madden *et al.* (2012) found evidence for six surface-rupturing events in the past 5600 yr along the western Garlock fault, 50 km from the San Andreas junction. Field *et al.* (2014) assign mean recurrence

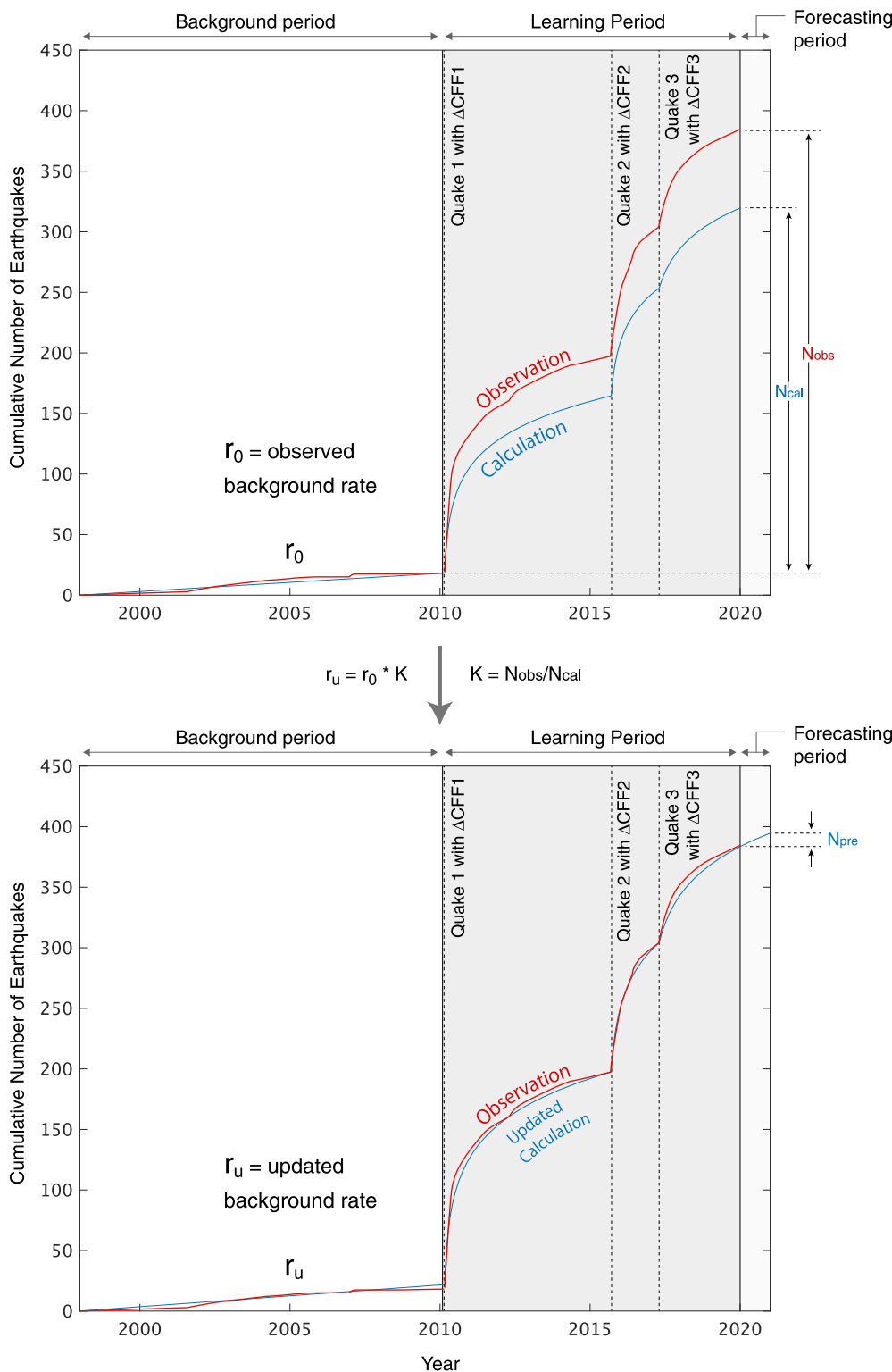


Figure 10. Schematic illustration of the observed and predicted seismicity rate behavior of one cell in a map area. The Learning Period, in which stress perturbations due to large quakes are considered, is used to modify the observed background rate (r_0) so that the net effect of all Learning Period quakes, given their local Coulomb stress changes, best matches the observed seismicity rate, and then fed back to correct background rate (r_u). Through this means, every cell affected by Learning Period earthquake has its background rate updated. The color version of this figure is available only in the electronic edition.

rates of 1230 yr (central section) and 1435 yr (western section) for the Garlock fault, based in part on these paleoseismic studies. If the stressed Garlock fault were to rupture from its junction with the Ridgecrest fault to its junction with the San Andreas, it would result in a 160 km long $M_w \sim 7.7$ earthquake, assuming 5 m of mean slip (based on Wells and Coppersmith, 1994) extending to depths of 11.5–15.0 km of the UCERF3 sources, and a shear modulus of 3×10^{11} dyn · cm. What is the chance that such a hypothetical event could trigger—either immediately or after some delay—a southern San Andreas of similar size?

In Figure 13, we calculate the static stress transferred by a Garlock fault rupture onto the San Andreas. We find a very large increase in failure stress on the Mojave section of the San Andreas, extending southeast from the Garlock junction, contrasting with an equally large stress decrease extending northwest from the junction on the San Andreas Big-Bend and Carrizo sections. So, a plausible—or at least not easily falsifiable—outcome of the Ridgecrest earthquake could be a very large rupture on the Garlock fault, followed by a Mojave section rupture of the San Andreas, either immediately, or after a delay. Here, we are ignoring the important dynamic stresses, which should also be considered. But the dynamic stress would only increase the short-term rupture probability on the San Andreas.

If a Garlock rupture were to stress the San Andreas as shown in Figure 13, the

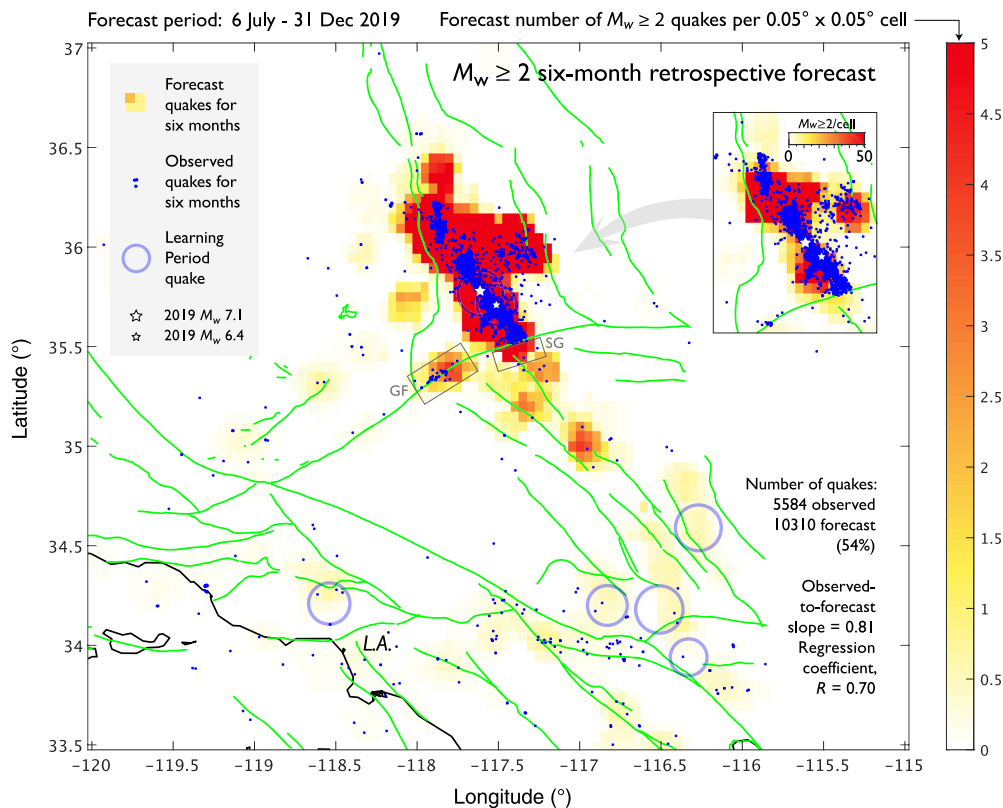


Figure 11. Retrospective forecast of $M_w \geq 2$ earthquakes during the first 6 months after the M_w 7.1 mainshock. An area with a successful forecast is GF (Garlock fault), and an unsuccessful forecast is SG (south of the Garlock). The inset shows the near-fault area at ten times higher stress saturation. The color version of this figure is available only in the electronic edition.

seismicity rate equation would forecast a roughly 150-fold increase in the probability of a Mojave section rupture. For this calculation, we use $A\sigma = 0.2$ bar and $t_a = 20$ yr, and a mean Coulomb stress change of 3 bars, as larger stress changes would only modestly increase the probability, and the actual slip on the Garlock fault might taper toward the San Andreas, unlike our uniform-slip model. In the most recent U.S. Geological Survey (USGS)-SCEC-California Geological Survey (CGS) California rupture model, the time-dependent UCERF3 (Field

et al., 2015), an M_w 7.7 Garlock fault rupture has a probability of 0.023% per year, and an M_w 7.7 Mojave section rupture of the San Andreas has a 0.33% per year probability. If that rupture terminated at the San Andreas junction, we calculate that it would raise the 1 yr probability of a San Andreas Mojave section M_w 7.7 rupture to 25%–67%. Combining these probabilities, we estimate a 1.15% chance (with range 0.58–1.50%) of a M_w 7.7 southern San Andreas rupture in the next year ($2.3\% \times 0.25$ – 0.67), an increase over its time-dependent UCERF3 rate by a factor of 3.5 (with range 2.7–4.6), as listed in Table 2. Compared to the time-independent version of UCERF3 (Field et al., 2014), which has a lower San Andreas probability, the chance of an M_w 7.7 would rise by a factor of 5.0.

We can compare our results to an independent 30-day forecast by Milner et al. (2020). They used an epidemic-type aftershock sequence model to make a retrospective forecast for the first 30 days after the M_w 7.1 Ridgecrest shock, estimating a 3.7% probability of a $M_w \geq 7$ Garlock rupture, and a 0.35% probability of an $M_w \geq 7$ San Andreas Mojave section rupture, although in their Figure 1c, they show an M_w 8.0 San Andreas rupture. When we recalculate our probabilities for their period, we find a 6.2% chance of a Garlock rupture, and a 3.0% chance of an M_w 7.7 San Andreas rupture, somewhat larger than theirs

TABLE 1
Large 1992–2019 Earthquakes Used for the Learning Period

Earthquake	Yr	Month	Day	Hr	Min	M_w	Finite-Fault Model
Joshua Tree	1992	4	23	4	4	6.2	Hough and Dreger (1995)
Landers	1992	6	28	11	11	7.3	Wald and Heaton (1994)
Big Bear	1992	6	28	15	15	6.5	Empirical (Wells and Coppersmith, 1994)
Big Pine	1993	5	17	23	23	6.1	Empirical (Wells and Coppersmith, 1994)
Northridge	1994	1	17	12	12	6.7	Wald et al. (1996)
Hector Mine	1999	10	16	9	9	7.1	Salichon et al. (2004)
Ridgecrest	2019	7	4	17	17	6.4	Xu et al. (2020)
Ridgecrest	2019	7	6	3	3	7.1	Xu et al. (2020)

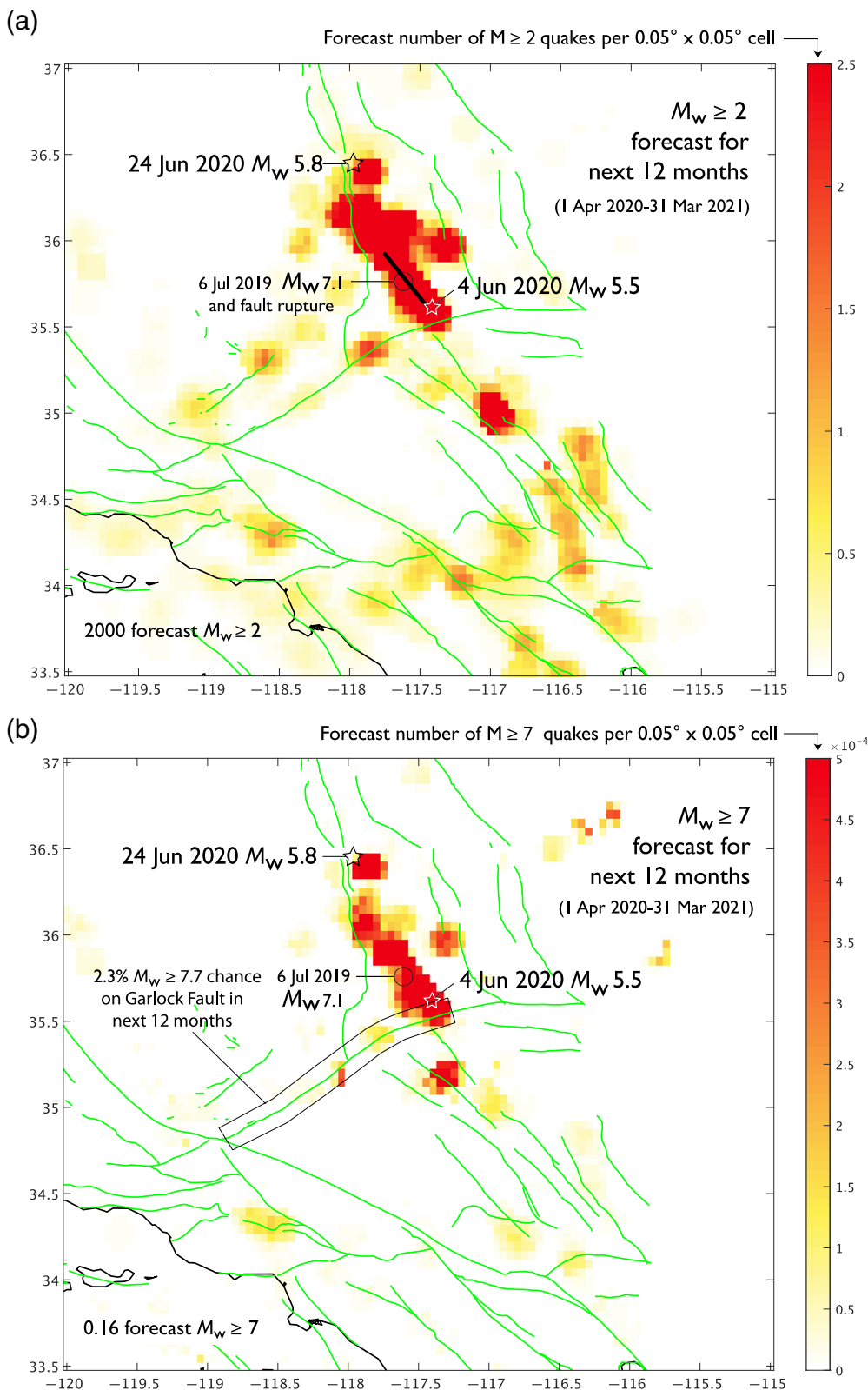


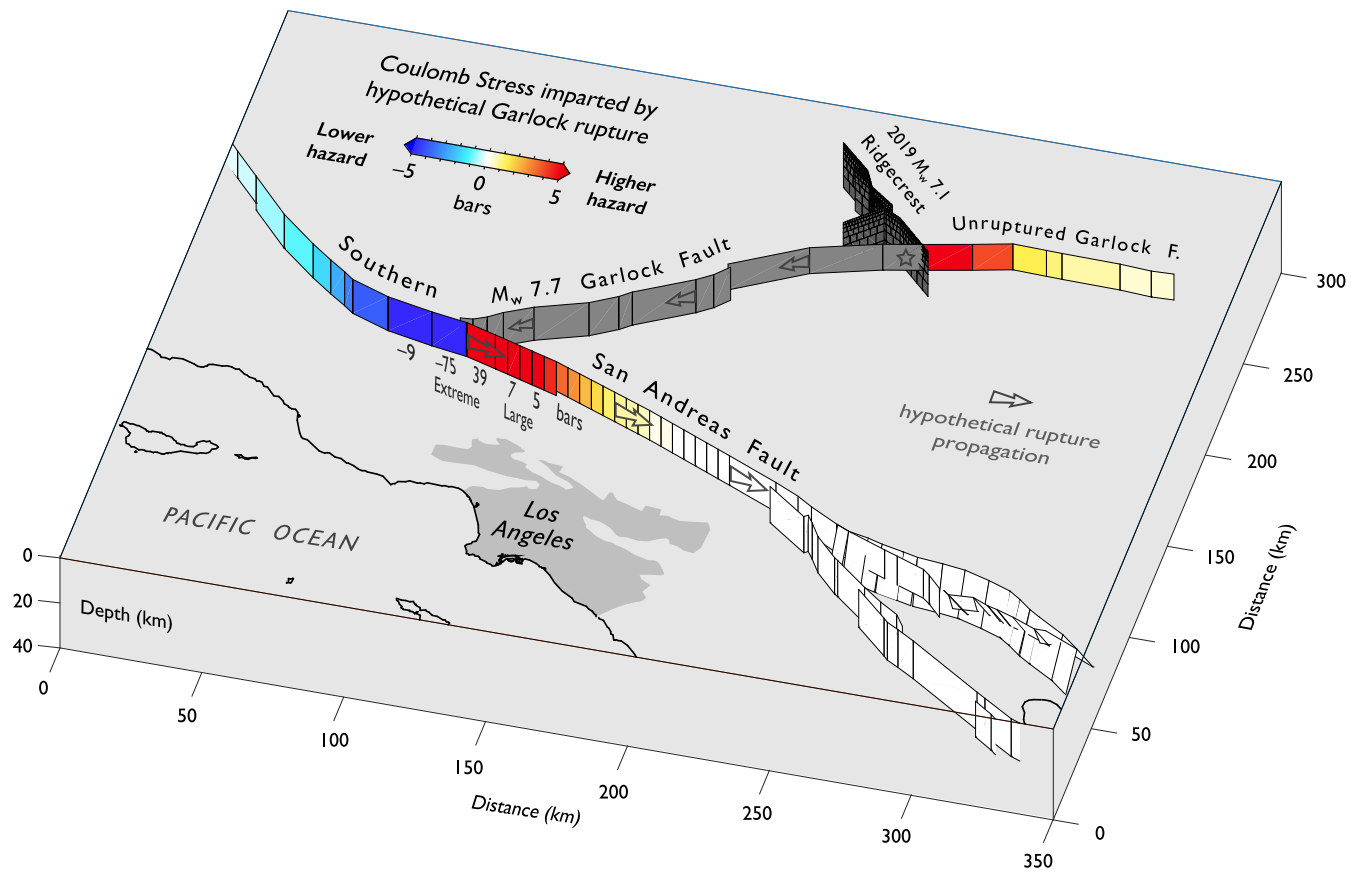
Figure 12. Prospective earthquake forecast for the next 12 months. (a) The $M_w \geq 2$ forecast does not use variable b -value information. The fading effects of large southern California earthquakes since 1992 (the Learning Period quakes shown in Fig. 11) are evident in the south. (b) The $M_w \geq 7$ forecast uses the spatial b -value information to scale up $M_w \geq 2$ rates to $M_w \geq 7$. The two $M_w > 5$ shocks that struck during the forecast period are both consistent with the forecast. The color version of this figure is available only in the electronic edition.

because of the stress transfer, and because in our model the probability of an M_w 7.7 is one-fifth of that of a M_w 7.0, whereas in theirs it is the same.

DISCUSSION

Our key finding is that when we try to incorporate the complexity of the Garlock fault, as represented by its associated focal mechanisms, the stress transfer from Ridgecrest appears simpler and more uniform than when we use the idealized planes of the SCEC Community Fault model or the UCERF3 surfaces. But it could be argued that because we are resolving the stress imparted to a diverse set of secondary faults, and because we choose the most positively stressed nodal plane for each mechanism, the uniformity in our result is the product of our selection criteria. So, could the Garlock fault still be better represented by the idealized planes?

Another solution would be to assume the Garlock fault zone friction was zero, in which case both nodal planes would have the same Coulomb stress change (Fig. S6). Low friction on the Garlock fault might, in fact, be the best assumption, for this reason: the Garlock has rotated clockwise over the past several million years (Nur *et al.*, 1993), and is now highly misaligned to the $\sim N7^\circ E$ principal compression axis, particularly along its eastern section (Savage *et al.*, 2001). Once the Eastern California Shear Zone becomes continuous and offsets the Garlock, the Garlock will become extinct. A similar geometry seems to apply to the east-striking Pinto Mountain



fault that is being offset by the north-northwest-oriented 1992 Landers rupture. Given its misalignment to the compression axis, the Garlock fault might only be able to slip if its friction were extremely low, in which case, Figure S6 could best represent the stress transfer. For zero friction, 82% of the central Garlock stress changes are positive for the M_w 6.4 shock; 96% of western Garlock stress changes are positive for the M_w 7.1 shock. Thus, the near-uniform increase in failure stress along the Garlock is found even when we remove the nodal plane ambiguity, and a stress increase on more than 100 km of the Garlock seems likely.

One might also argue that secondary faults captured by focal mechanisms, some at high angles to the main Garlock fault, have nothing to do with the triggering of large earthquakes, and so are irrelevant. But there is abundant evidence of large earthquakes nucleating on just such secondary faults,

Figure 13. The impact of a hypothetical Garlock rupture on the San Andreas fault. The arrows are not an explicit part of the model; rather, they convey what we consider to be a plausible sequence of events. Stress imparted to focal mechanisms along the San Andreas is shown in Figure S7; the impact of shorter Garlock ruptures on the San Andreas are shown in Figure S8. The color version of this figure is available only in the electronic edition.

which then propagate onto the main fault. Examples include the 2001 M_w 7.8 Kunlun (Ozacar and Beck, 2004), 2002 M_w 7.9 Denali (Eberhart-Phillips *et al.*, 2003), 2010 M_w 7.2 El Mayor-Cucapah (Hauksson *et al.*, 2011; Wei *et al.*, 2011; Segou and Parsons, 2020), 2016 M_w 7.8 Kaikōura (Xu *et al.*, 2018), and perhaps also the 2011 M_w 9.0 Tohoku (Chu *et al.*, 2011) earthquakes. Cascading nucleation from secondary faults may even be common.

TABLE 2
Annual Large Earthquake Probabilities

$M_w \geq 7.7$ Fault Rupture	Background Probability (Time-Dep. UCERF3)	Probability during Next 12 Months (This Study)	Probability Increase over Time-Dep. UCERF3
Garlock (west + central sections)	0.023%	2.3%	100
San Andreas (Mojave section)	0.33%	1.15%	3.5
San Andreas range		0.58–1.50%	2.7–4.6

UCERF3, Uniform California Earthquake Rupture Forecast version 3.

What if the Garlock ruptured in an earthquake that did not reach the San Andreas fault? We find that a rupture that terminates 45 km or less from the San Andreas ($M_w \geq 7.5$) is large enough to increase the Mojave section rupture probability by a factor of 150, about the same as a full rupture of the fault. In contrast, events that terminate 90 km or more from the San Andreas only increase the Mojave section ($M_w < 7.5$) rupture probability by a factor of 10 or less (Fig. S8).

Finally, isn't it hypocritical to resolve the stresses imparted by a hypothetical Garlock fault rupture in Figure 13 onto the idealized San Andreas fault, given our claim that near-fault focal mechanisms better reflect the stress transfer than idealized planes? And the UCERF3 idealization might be unusually inadequate here, because Fuis *et al.* (2012) argue that the southern San Andreas is not vertical, but dips southwest near the Garlock junction, and dips northeast near San Bernardino Mountain. Although for simplicity of presentation, we show an idealized San Andreas in Figure 13, we also calculated the Garlock stresses onto San Andreas focal mechanisms in Figure S7, which yields much the same result: A 25 km long San Andreas section extending southeast of the Garlock junction with stress increase of >25 bars, contrasted with a 60 km long section extending northwest of the junction with stress decrease of >5 bars. So, both ways of representing the San Andreas suggest earthquake promotion of the section to the southeast of the junction (the Mojave section), and earthquake inhibition of the section to the northwest of the junction (Carrizo section).

CONCLUSIONS

The Ridgecrest sequence affords a unique opportunity to probe earthquake interaction on time scales of 150 yr to 30 hr; on distance scales of 5–150 km, and on magnitude scales from M_w 2 to M_w 7. We present evidence that earthquake promotion and inhibition are at least partly explained by static Coulomb stress changes, with interaction of the M_w 6.4 and M_w 7.1 mainshocks of the Ridgecrest sequence furnishing the strongest evidence. The method we presented to forecast earthquake occurrence seeks to incorporate the complexity of fault zone networks through focal mechanisms. Ironically, when viewed this way, the Garlock fault stressing is much simpler and more uniform than when we resolve the stress on an idealized contiguous planar surface, for which ~ 120 km of the fault was brought closer to failure. Although assessing the likelihood of a major Garlock rupture and its consequences for a San Andreas earthquake are difficult and speculative, it is important enough that we have sought to estimate it. We calculate a 1.15% probability of an $M_w \geq 7.7$ on the Mojave section of the San Andreas during the 12 months beginning 1 April 2020, which is about 3.5 times higher than its time-dependent UCERF3 probability, and 5.0 times higher than its time-independent UCERF3 probability.

DATA AND RESOURCES

The finite-fault source model (Xu *et al.*, 2020) was accessed from https://topex.ucsd.edu/SV_7.1/index.html (last accessed November 2019), and was then converted to Earthquake Source Model Database (SRCMOD) database format, which is available from the following two URLs, for the M_w 6.4 and M_w 7.1 earthquakes, respectively: <http://equake-rc.info/SRCMOD/searchmodels/viewmodel/s2019RIDGEC01XUxx/> and <http://equake-rc.info/SRCMOD/searchmodels/viewmodel/s2019RIDGEC02XUxx/> (last accessed April 2020). We used the hypocenter catalog of the Southern California Earthquake Center (SCEC) relocated via the Hauksson *et al.* (2012), at <https://scedc.caltech.edu/research-tools/alt-2011-dd-hauksson-yang-shearer.html> (last accessed April 2020). We used the focal mechanism catalog of SCEC made via Yang *et al.* (2012): <https://scedc.caltech.edu/research-tools/alt-2011-yang-hauksson-shearer.html> (last accessed April 2020). The authors accessed the Uniform California Earthquake Rupture Forecast version 3 (UCERF3)-time-dependent probabilities (Field *et al.*, 2015) via their Figure 10, and also via http://opensha.usc.edu/ftp/kmilner/ucerf3/ucerf3_timedep_30yr_probs.kmz (last accessed April 2020). We used Coulomb 3.4 (Toda *et al.*, 2005) for stress calculations, available at <https://earthquake.usgs.gov/research/software/coulomb/> (last accessed April 2020). For magnitude of completeness calculations, we used ZMAP (Wiemer, 2001), available at <http://www.seismo.ethz.ch/en/research-and-teaching/products-software/software/ZMAP/> (last accessed April 2020). The authors also include supplemental material with seven figures that provide additional supporting evidence for statements made in the article, and also provide alternative ways of examining the data for completeness.

ACKNOWLEDGMENTS

The authors are indebted to Kiran Kumar Thingbaijam, Benjamín Idini, and Martin Mai for meticulously translating the Ross *et al.* (2019) and Xu *et al.* (2020) source models into SRCMOD format. The authors thank Kenneth Hudnut, Timothy Dawson, Volkan Sevilgen, Myrto Papaspiliou, Rosa Sobradelo Pérez, Crescenzo Petrone, and Alexandra Tsioulou for their probing reviews and scientific insights. The authors gratefully acknowledge grants from the Willis Research Network and the Small Business Innovation Research program of the U.S. National Science Foundation.

REFERENCES

- Aki, K. (1965). Maximum likelihood estimate of b in the formula $\log N = a - bM$ and its confidence limits, *Bull. Earthq. Res. Inst. Tokyo Univ.* **43**, 237–239.
- Barnhart, W. D., G. P. Hayes, and R. D. Gold (2019). The July 2019 Ridgecrest, California, earthquake sequence: Kinematics of slip and stressing in cross-fault ruptures, *Geophys. Res. Lett.* **46**, no. 21, doi: [10.1029/2019GL084741](https://doi.org/10.1029/2019GL084741).
- Bawden, G. W. (2001). Source parameters for the 1952 Kern County earthquake, California: A joint inversion of leveling and triangulation observations, *J. Geophys. Res.* **106**, no. B1, 771–785, doi: [10.1029/2000JB900315](https://doi.org/10.1029/2000JB900315).
- Beanland, S., and M. M. Clark (1994). The Owens Valley fault zone, eastern California, and surface faulting associated with the 1872 earthquake, *U.S. Geol. Surv. Bull.* **1982**, 29, doi: [10.3133/b1982](https://doi.org/10.3133/b1982).

- Brodsky, E. E. (2006). Long-range triggered earthquakes that continue after the wave train passes, *Geophys. Res. Lett.* **33**, no. 15, doi: [10.1029/2006GL026605](https://doi.org/10.1029/2006GL026605).
- Chu, R., S. Wei, D. V. Helmberger, Z. Zhan, L. Zhu, and H. Kanamori (2011). Initiation of the great M_w 9.0 Tohoku–Oki earthquake, *Earth Planet. Sci. Lett.* **308**, nos. 3/4, 277–283, doi: [10.1016/j.epsl.2011.06.031](https://doi.org/10.1016/j.epsl.2011.06.031).
- Dawson, T. E., S. F. McGill, and T. K. Rockwell (2003). Irregular recurrence of paleoearthquakes along the central Garlock fault near El Paso Peaks, California, *J. Geophys. Res.* **108**, no. B7, 2356, doi: [10.1029/2001JB001744](https://doi.org/10.1029/2001JB001744).
- DeVries, P. M. R., F. Viégas, M. Wattenberg, and B. J. Meade (2018). Deep learning of aftershock patterns following large earthquakes, *Nature* **560**, 632–634, doi: [10.1038/s41586-018-0438-y](https://doi.org/10.1038/s41586-018-0438-y).
- Dieterich, J. H. (1994). A constitutive law for the rate of earthquake production and its application to earthquake clustering, *J. Geophys. Res.* **99**, no. B2, 2601–2618, doi: [10.1029/93JB02581](https://doi.org/10.1029/93JB02581).
- Dreger, D., and A. Kaverina (2000). Seismic remote sensing for the earthquake source process and near source strong shaking, a case study of the October 16, 1999 Hector Mine earthquake, *Geophys. Res. Lett.* **27**, no. 13, 1941–1944, doi: [10.1029/1999GL011245](https://doi.org/10.1029/1999GL011245).
- Eberhart-Phillips, D., P. J. Haeussler, J. T. Freymueller, A. D. Frankel, C. M. Rubin, P. Craw, N. A. Ratchkovski, G. Anderson, G. A. Carver, A. J. Crone, *et al.* (2003). The 2002 Denali fault earthquake, Alaska: A large magnitude, slip-partitioned event, *Science* **300**, no. 5622, 1113–1118, doi: [10.1126/science.1082703](https://doi.org/10.1126/science.1082703).
- Ekström, G., M. Nettles, and A. M. Dziewonski (2012). The Global CMT project 2004–2010: Centroid-moment tensors for 13,017 earthquakes, *Phys. Earth Planet. In.* **200/201**, nos. 200/201, 1–9, doi: [10.1016/j.pepi.2012.04.002](https://doi.org/10.1016/j.pepi.2012.04.002).
- Field, E. H., R. J. Arrowsmith, G. P. Biasi, P. Bird, T. E. Dawson, K. R. Felzer, D. D. Jackson, K. M. Johnson, T. H. Jordan, C. M. Andrew, *et al.* (2014). Uniform California Earthquake Rupture Forecast, Version 3 (UCERF3), the time-independent model, *Bull. Seismol. Soc. Am.* **104**, no. 3, 1122–1180, doi: [10.1785/0120130164](https://doi.org/10.1785/0120130164).
- Field, E. H., G. P. Biasi, P. Bird, T. E. Dawson, K. R. Felzer, D. D. Jackson, K. M. Johnson, T. H. Jordan, C. Madden, A. J. Michael, *et al.* (2015). Long-term time-dependent probabilities for the Third Uniform California Earthquake Rupture Forecast (UCERF3), *Bull. Seismol. Soc. Am.* **105**, no. 2A, 511–543, doi: [10.1785/0120140093](https://doi.org/10.1785/0120140093).
- Fuis, G. S., D. S. Scheirer, V. E. Langenheim, and M. D. Kohler (2012). A new perspective on the geometry of the San Andreas fault in southern California and its relationship to lithospheric structure, *Bull. Seismol. Soc. Am.* **102**, no. 1, 236–251, doi: [10.1785/0120110041](https://doi.org/10.1785/0120110041).
- Goldberg, D. E., D. Melgar, V. J. Sahakian, A. M. Thomas, X. Xu, B. W. Crowell, and J. Geng (2020). Complex rupture of an immature fault zone: A simultaneous kinematic model of the 2019 Ridgecrest, CA earthquakes, *Geophys. Res. Lett.* **47**, no. 3, doi: [10.1029/2019GL086382](https://doi.org/10.1029/2019GL086382).
- Grant, L. B., and A. Donnellan (1994). 1855 and 1991 surveys of the San Andreas fault: Implications for fault mechanics, *Bull. Seismol. Soc. Am.* **84**, no. 2, 241–246.
- Grant, L. B., and K. E. Sieh (1993). Stratigraphic evidence for seven meters of dextral slip on the San Andreas fault during the 1857 earthquake in the Carrizo Plain, *Bull. Seismol. Soc. Am.* **83**, no. 3, 619–635.
- Hardebeck, J. L., J. J. Nazareth, and E. Hauksson (1998). The static stress change triggering model: Constraints from two southern California aftershock sequences, *J. Geophys. Res.* **103**, doi: [10.1029/98JB00573](https://doi.org/10.1029/98JB00573).
- Harris, R. A. (1998). Introduction to special section: Stress triggers, stress shadows, and implications for seismic hazard, *J. Geophys. Res.* **103**, no. B10, 24,347–24,358, doi: [10.1029/98JB01576](https://doi.org/10.1029/98JB01576).
- Hauksson, E., J. Stock, K. Hutton, W. Yang, J. A. Vidal-Villegas, and H. Kanamori (2011). The 2010 M_w 7.2 El Mayor-Cucapah earthquake sequence, Baja California, Mexico and southernmost California, USA: Active seismotectonics along the Mexican Pacific margin, *Pure Appl. Geophys.* **168**, 1255–1277, doi: [10.1007/s00024-010-0209-7](https://doi.org/10.1007/s00024-010-0209-7).
- Hauksson, E., W. Yang, and P. M. Shearer (2012). Waveform relocated earthquake catalog for southern California (1981 to 2011), *Bull. Seismol. Soc. Am.* **102**, no. 5, 2239–2244, doi: [10.1785/0120120010](https://doi.org/10.1785/0120120010).
- Hill, D. P. (2008). Dynamic stresses, Coulomb failure, and remote triggering, *Bull. Seismol. Soc. Am.* **98**, no. 1, 66–92, doi: [10.1785/0120070049](https://doi.org/10.1785/0120070049).
- Hough, S. E., and D. S. Dreger (1995). Source parameters of the 23 April 1992 M 6.1 Joshua Tree, California, earthquake and its aftershocks; empirical Green's function analysis of GEOS and TERRAScope data, *Bull. Seismol. Soc. Am.* **85**, no. 6, 1576–1590.
- Hough, S. E., and K. Hutton (2008). Revisiting the 1872 Owens Valley, California, earthquake, *Bull. Seismol. Soc. Am.* **98**, no. 2, 931–949, doi: [10.1785/0120070186](https://doi.org/10.1785/0120070186).
- Hudnut, K. W., L. Seeber, and J. Pacheco (1989). Cross-fault triggering in the November 1987 Superstition Hills Earthquake Sequence, southern California, *Geophys. Res. Lett.* **16**, no. 2, 199–202, doi: [10.1029/GL016i002p00199](https://doi.org/10.1029/GL016i002p00199).
- Kilb, D. (2003). A strong correlation between induced peak dynamic Coulomb stress change from the 1992 M 7.3 Landers, California, earthquake and the hypocenter of the 1999 M 7.1 Hector Mine, California, earthquake, *J. Geophys. Res.* **108**, no. B1, doi: [10.1029/2001JB000678](https://doi.org/10.1029/2001JB000678).
- King, G. C. P., R. S. Stein, and J. Lin (1994). Static stress changes and the triggering of earthquakes, *Bull. Seismol. Soc. Am.* **84**, no. 3, 935–953.
- Lin, J., and R. S. Stein (2004). Stress triggering in thrust and subduction earthquakes and stress interaction between the southern San Andreas and nearby thrust and strike-slip faults, *J. Geophys. Res.* **109**, no. B2, B02303, doi: [10.1029/2003JB002607](https://doi.org/10.1029/2003JB002607).
- Ma, K.-F., C.-H. Chan, and R. S. Stein (2005). Response of seismicity to Coulomb stress triggers and shadows of the 1999 M_w = 7.6 Chi-Chi, Taiwan, earthquake, *J. Geophys. Res.* **110**, no. B5, doi: [10.1029/2004JB003389](https://doi.org/10.1029/2004JB003389).
- Madden Madugo, C., J. F. Dolan, and R. D. Hartleb (2012). New paleoearthquake ages from the Western Garlock fault: Implications for regional earthquake occurrence in Southern California, *Bull. Seismol. Soc. Am.* **102**, no. 6, 2282–2299, doi: [10.1785/0120110310](https://doi.org/10.1785/0120110310).
- Mallman, E. P., and M. D. Zoback (2007). Assessing elastic Coulomb stress transfer models using seismicity rates in southern California and southwestern Japan, *J. Geophys. Res.* **112**, no. B3, doi: [10.1029/2005JB004076](https://doi.org/10.1029/2005JB004076).
- McGill, S., and K. Sieh (1993). Holocene slip rate of the central Garlock fault in the southeastern Searles Valley, California, *J. Geophys. Res.* **98**, no. B8, 14,217–14,231, doi: [10.1029/93JB00442](https://doi.org/10.1029/93JB00442).
- Milner, K. R., E. H. Field, W. H. Savran, M. T. Page, and T. H. Jordan (2020). Operational earthquake forecasting during the 2019 Ridgecrest,

- California, earthquake sequence with the UCERF3-ETAS Model, *Seismol. Res. Lett.* **93**, no. 3, 1–12, doi: [10.1785/0220190294](https://doi.org/10.1785/0220190294).
- Monastero, F. C., A. E. Sabin, and J. D. Walker (1997). Evidence for post-early Miocene initiation of movement on the Garlock fault from offset of the Cudahy Camp Formation, east-central California, *Geology* **25**, no. 3, 247–250, doi: [10.1130/0091-7613](https://doi.org/10.1130/0091-7613).
- Nur, A., H. Ron, and G. C. Beroza (1993). The nature of the Landers-Mojave earthquake line, *Science* **261**, no. 5118, 201–203, doi: [10.1126/science.261.5118.201](https://doi.org/10.1126/science.261.5118.201).
- Ozcar, A. A., and S. L. Beck (2004). The 2002 Denali fault and 2001 Kunlun fault earthquakes: Complex rupture processes of two large strike-slip events, *Bull. Seismol. Soc. Am.* **94**, S278–S292, doi: [10.1785/0120040604](https://doi.org/10.1785/0120040604).
- Parsons, T. (2002). Global Omori law decay of triggered earthquakes: Large aftershocks outside the classical aftershock zone, *J. Geophys. Res.* **107**, no. B9, doi: [10.1029/2001JB000646](https://doi.org/10.1029/2001JB000646).
- Parsons, T., Y. Ogata, J. Zhuang, and E. L. Geist (2012). Evaluation of static stress change forecasting with prospective and blind tests, *Geophys. J. Int.* **188**, no. 3, 1425–1440, doi: [10.1111/j.1365-246X.2011.05343.x](https://doi.org/10.1111/j.1365-246X.2011.05343.x).
- Plesch, A., J. H. Shaw, C. Benson, W. A. Bryant, S. Carena, M. Cooke, J. Dolan, G. Fuis, E. Gath, L. Grant, *et al.* (2007). Community Fault Model (CFM) for Southern California, *Bull. Seismol. Soc. Am.* **97**, no. 6, 1793–1802, doi: [10.1785/0120050211](https://doi.org/10.1785/0120050211).
- Pollitz, F. F., R. S. Stein, V. Sevilgen, and R. Bürgmann (2012). The 11 April 2012 east Indian Ocean earthquake triggered large aftershocks worldwide, *Nature* **490**, 250–253, doi: [10.1038/nature11504](https://doi.org/10.1038/nature11504).
- Richards-Dinger, K., and J. H. Dieterich (2012). RSQSim Earthquake Simulator, *Seismol. Res. Lett.* **83**, no. 6, 983–990, doi: [10.1785/0220120105](https://doi.org/10.1785/0220120105).
- Rollins, C., R. S. Stein, G. Lin, and D. Kilb (2019). The Ridgecrest earthquakes: Torn ground, nested foreshocks, Garlock shocks, and Temblor's forecast, *Temblor*, doi: [10.32858/temblor.039](https://doi.org/10.32858/temblor.039).
- Ross, Z. E., B. Indini, Z. Jia, O. L. Stephenson, M. Zhong, X. Wang, Z. Zhan, M. Simons, E. J. Fielding, S.-H. Yon, *et al.* (2019). Hierarchical interlocked orthogonal faulting in the 2019 Ridgecrest earthquake sequence, *Science* **366**, no. 6463, 346–351, doi: [10.1126/science.aaz0109](https://doi.org/10.1126/science.aaz0109).
- Salichon, J., P. Lundgren, B. Delouis, and D. Giardini (2004). Slip History of the 16 October 1999 Mw 7.1 Hector Mine earthquake (California) from the inversion of InSAR, GPS, and teleseismic data, *Bull. Seismol. Soc. Am.* **94**, no. 6, 2015–2027, doi: [10.1785/0120030038](https://doi.org/10.1785/0120030038).
- Savage, J. C., and M. Lisowski (1995). Strain accumulation in Owens Valley, California, 1974 to 1988, *Bull. Seismol. Soc. Am.* **85**, no. 12, 151–158, doi: [10.1029/GL017i012p02113](https://doi.org/10.1029/GL017i012p02113).
- Savage, J. C., W. Gan, and J. L. Svarc (2001). Strain accumulation and rotation in the Eastern California Shear Zone, *J. Geophys. Res.* **106**, no. B10, 21,995–22,007, doi: [10.1029/2000JB000127](https://doi.org/10.1029/2000JB000127).
- Segou, M., and T. Parsons (2020). A new technique to calculate earthquake stress transfer and to probe the physics of aftershocks, *Bull. Seismol. Soc. Am.* **110**, no. 2, 863–873, doi: [10.1785/0120190033](https://doi.org/10.1785/0120190033).
- Stacy, S., M. Gerstenberger, C. Williams, D. Rhoades, and A. Christophersen (2014). A new hybrid Coulomb/statistical model for forecasting aftershock rates, *Geophys. J. Int.* **196**, no. 2, 918–923, doi: [10.1093/gji/ggt404](https://doi.org/10.1093/gji/ggt404).
- Stein, R. S. (1999). The role of stress transfer in earthquake occurrence, *Nature* **402**, 605–609, doi: [10.1038/45144](https://doi.org/10.1038/45144).
- Stein, R. S., and W. Thatcher (1981). Seismic and aseismic deformation associated with the 1952 Kern County, California, earthquake and relationship to the Quaternary history of the White Wolf fault, *J. Geophys. Res.* **86**, no. B6, 4913–4928, doi: [10.1029/JB086iB06p04913](https://doi.org/10.1029/JB086iB06p04913).
- Toda, S., and R. S. Stein (2003). Toggling of seismicity by the 1997 Kagoshima earthquake couplet: A demonstration of time-dependent stress transfer, *J. Geophys. Res.* **108**, 2567, doi: [10.1029/2003JB002527](https://doi.org/10.1029/2003JB002527).
- Toda, S., and R. S. Stein (2019). Ridgecrest earthquake shut down cross-fault aftershocks, *Temblor*, doi: [10.32858/temblor.043](https://doi.org/10.32858/temblor.043).
- Toda, S., R. S. Stein, G. C. Beroza, and D. Marsan (2012). Aftershocks halted by static stress shadows, *Nat. Geosci.* **5**, 410–413, doi: [10.1038/ngeo1465](https://doi.org/10.1038/ngeo1465).
- Toda, S., R. S. Stein, K. Richards-Dinger, and S. B. Bozkurt (2005). Forecasting the evolution of seismicity in southern California: Animations built on earthquake stress transfer, *J. Geophys. Res.* **110**, no. B05S16, doi: [10.1029/2004JB003415](https://doi.org/10.1029/2004JB003415).
- Wald, D. J., and T. H. Heaton (1994). Spatial and temporal distribution of slip for the 1992 Landers, California, Earthquake, *Bull. Seismol. Soc. Am.* **84**, no. 3, 668–691.
- Wald, D. J., T. H. Heaton, and K. W. Hudnut (1996). The slip history of the 1994 Northridge, California, earthquake determined from strong-motion, teleseismic, GPS, and leveling data, *Bull. Seismol. Soc. Am.* **86**, no. 1B, S49–S70.
- Wei, S., E. Fielding, S. Leprince, A. Sladen, J.-P. Avouac, D. Helmberger, E. Hauksson, R. Chu, M. Simons, K. Hudnut, *et al.* (2011). Superficial simplicity of the 2010 El Mayor–Cucapah earthquake of Baja California in Mexico, *Nat. Geosci.* **4**, 615–618, doi: [10.1038/ngeo1213](https://doi.org/10.1038/ngeo1213).
- Wells, D. L., and K. J. Coppersmith (1994). New empirical relationships among magnitude, rupture length, rupture width, rupture area, and surface displacement, *Bull. Seismol. Soc. Am.* **84**, no. 4, 974–1002.
- Wiemer, S. (2001). A software package to analyse seismicity: ZMAP, *Seismol. Res. Lett.* **72**, no. 3, 373–382, doi: [10.1785/gssrl.72.3.373](https://doi.org/10.1785/gssrl.72.3.373).
- Woessner, J., and S. Wiemer (2005). Assessing the quality of earthquake catalogues: Estimating the magnitude of completeness and its uncertainty, *Bull. Seismol. Soc. Am.* **95**, no. 2, 684–698, doi: [10.1785/0120040007](https://doi.org/10.1785/0120040007).
- Xu, W., G. Feng, L. Meng, A. Zhang, J. P. Ampuero, R. Bürgmann, and L. Fang (2018). Transpressional rupture cascade of the 2016 Mw 7.8 Kaikoura earthquake, New Zealand, *J. Geophys. Res.* **123**, no. 3, 2396–2409, doi: [10.1002/2017JB015168](https://doi.org/10.1002/2017JB015168).
- Xu, X., D. T. Sandwell, and B. Smith-Konter (2020). Coseismic displacements and surface fractures from Sentinel-1 InSAR: 2019 Ridgecrest earthquakes, *Seismol. Res. Lett.* doi: [10.1785/0220190275](https://doi.org/10.1785/0220190275).
- Yang, W., E. Hauksson, and P. M. Shearer (2012). Computing a large refined catalog of focal mechanisms for southern California (1981–2010): Temporal stability of the style of faulting, *Bull. Seismol. Soc. Am.* **102**, no. 3, 1179–1194, doi: [10.1785/0120110311](https://doi.org/10.1785/0120110311).
- Zielke, O., J. R. Arrowsmith, L. G. Ludwig, and S. O. Akciz (2012). High-resolution topography-derived offsets along the 1857 Fort Tejon earthquake rupture trace, San Andreas fault, *Bull. Seismol. Soc. Am.* **102**, no. 3, 1135–1154, doi: [10.1785/0120110230](https://doi.org/10.1785/0120110230).